A Multifunctional Molecular Bridging Layer for High Efficiency, Hysteresis-Free, and Stable Perovskite Solar Cells

Yin, Li; Ding, Changzeng; Liu, Chenguang; Zhao, Chun; Zha, Wusong; Mitrovic, Ivona Z.; Lim, Eng Gee; Han, Yunfei; Gao, Xiaomei; Zhang, Lianping; Wang, Haibin; Li, Yuanxi; Wilken, Sebastian; Österbacka, Ronald; Lin, Hongzhen; Ma, Chang-Qi; Zhao, Cezhou

Published in:
Advanced Energy Materials

DOI:
10.1002/aenm.202301161
10.1002/aenm.202301161

Published: 07/07/2023

Document Version
Accepted author manuscript

Document License
All rights reserved

A multifunctional molecular bridging layer for high efficiency, hysteresis-free and stable perovskite solar cells

Li Yin, Changzeng Ding, Chenguang Liu, Chun Zhao, Wusong Zha, Ivona Z. Mitrovic, Eng Gee Lim*, Yunfei Han, Lianping Zhang, Haibin Wang, Yuanxi Li, Sebastian Wilken, Ronald Österbacka, Hongzhen Lin, Chang-Qi Ma* and Cezhou Zhao*

Dr. Li Yin, Haibin Wang, Yuanxi Li, Dr. Chun Zhao, Prof. E. G. Lim, Prof. C. Z. Zhao
School of Advanced Technology, Xi'an Jiaotong-Liverpool University, Renai Road, Suzhou 215123 China
E-mail: chun.zhao@xjtlu.edu.cn; enggee.lim@xjtlu.edu.cn

Dr. Li Yin, Haibin Wang, Dr. Chun Zhao, Prof. E. G. Lim
Department of Electrical Engineering and Electronics, University of Liverpool, Liverpool L69 72Z, UK

Dr. Changzeng Ding, Wusong Zha, Dr. Yunfei Han, Lianping Zhang, Prof. Ronald Österbacka, Prof. Hongzhen Lin, Prof. Chang-Qi Ma
i-lab & Printable Electronics Research Center, Suzhou Institute of Nano-Tec and Nano-Bionics, Chinese Academy of Sciences (CAS), 398 Ruoshui Road, SEID, SIP, Suzhou 215123, P. R. China
E-mail: cqma2011@sinano.ac.cn

Dr. Chenguang Liu
School of Robotics
Xi'an Jiaotong-Liverpool University, Renai Road, Suzhou 215123, China

Dr. I. Z. Mitrovic
Department of Electrical Engineering and Electronics
University of Liverpool, Liverpool L69 3GJ, UK

Prof. Ronald Österbacka, Dr. Sebastian Wilken
Physics and Center for Functional Materials, Faculty of Science and Engineering, Åbo Akademi University, Henriksgatan 3, 20500 Turku, Finland

Keywords: multifunctional molecular bridging layer; hysteresis-free; Li^+ ions migration; high moisture and operation stability.

At present, the dominating electron transport material (ETL) and hole transport material (HTL) used in the state-of-the-art perovskite solar cells (PSCs) are tin oxide (SnO_2) and 2,2′,7,7′-tetrakis (N, N-di-pmethoxyphenylamine)-9,9′-spirobifluorene (Spiro-OMeTAD). However, the surface hydroxyl groups of the SnO_2 layer and the Li^+ ions within the Spiro-OMeTAD HTL layer generally cause surface charge recombination and Li^+ migrations, significantly reducing the device's performance and stability. Here, we introduce a molecule bridging layer of 3,5-bis(fluorosulfonyl)benzoic acid (FBA) onto the SnO_2 surface, which provides appropriate surface energy, reduces interfacial traps, forms a better energy level alignment, and, most importantly, anchors (immobilizes) Li^+ ions in the ETL, and consequently improved the device power conversion efficiency (PCE) up to 24.26% without hysteresis. Moreover, the device with the FBA passivation layer shows excellent moisture and operational stability, maintaining over 80% of the initial PCE after 1000 h under both aging conditions. The current work provides a comprehensive understanding of the influence of the extrinsic Li^+ ion migration within the cell on the device's performance and stability, which helps design and fabricate high-performance and hysteresis-free PSCs.

1. Introduction

Organic-inorganic halide perovskite solar cells (PSCs) have great potential for next-generation solar cells due to their long charge-carrier diffusion length, wide absorption range, tunable energy bandgap, and low-cost and low-energy solution

processing.[1-5] So far, the power conversion efficiency (PCE) of single-junction perovskite solar cells has reached 25.7%,[6] which is close to the silicon heterojunction solar cell record.[7] The most used electron-transport material (ETL) and hole-transport material (HTL) in the state-of-the-art PSCs are tin oxide (SnO_2) and lithium bis-(trifluoromethanesulfonyl) imide salt (LiTFSI) doped 2,2′,7,7′-tetrakis(*N*, *N*-di-(*p*-methoxyphenylamino))-9,9′-spirobifluorene (Spiro-OMeTAD), respectively. However, there are still some issues with these materials for commercialization.

For the SnO_2 ETL, some unavoidable charge-trap states, including hydroxy, oxygen, tin vacancies, interstitials, surface hydroxyl groups, and anti-site defects,[8] exist in bulk and at the interface between the ETL and the perovskite layer. These charge-trap states act as recombination centers, leading to increased non-radiative recombination, reducing the PCE and stability of the devices. Hence, some passivation methods have been extensively investigated for bulk SnO_2 and the interface between the SnO_2 and active layer. The passivation methods include doping using ionic compounds.[9] acid treatments,[10] bilayer ETL formation,[11] and the use of polymer as additive[12] and buffer layers.[13] The molecular bridging layer can be very promising considering a method of simultaneously controlling the surface roughness, work function alignment, trap passivation, and the mechanical reliability interface modification leading to non-radiative recombination and instability. Yang and coworkers indicated that a 3-aminopropyltriethoxysilane (APTES) self-assembled molecules (SAM) as an interfacial layer could modify the interface, enhancing the interfacial contact and improving the morphology and crystallinity of perovskite

films.[14] Wang et al. reported that C_{60}-SAM facilitates electron transfer from the perovskite layer to the SnO_2 ETL due to its high electron affinity.[15] Dong et al. found that the novel 2,4,5-trichlorobenzenesulfonic acid potassium salt (3Cl-BSAK) could eliminate the device hysteresis and the V_{OC} loss due to the efficient interaction between carbon-chlorine bonds with uncoordinated Sn, effectively filling oxygen vacancies in the SnO_2 surface.[16] Dai et al. demonstrated an iodine-terminated self-assembled monolayer (I-SAM) used in perovskite solar cells (PSCs) to achieve a 50% increase in adhesion toughness at the interface between the ETL and the halide perovskite thin film to enhance mechanical reliability. These successful examples suggest that interfacial engineering with multifunctional molecule is a great option to enhance the PCE and stability of the n-i-p PSCs with SnO_2 ETL.

On the other hand, for Spiro-OMeTAD HTL, some chemical dopants such as tertbutylpyridine (TBP) and lithium bis -(trifluoromethanesulfonyl) imide salt (LiTFSI) are indispensable to achieving efficient hole extraction and sufficient conductivity.[17] These deliquescent dopants have a profound negative influence on the stability of the PCSs, due to the hygroscopicity of lithium salt and the migratory nature of Li^+ ions.[18, 19] Li^+ ions could migrate from spiro-OMeTAD to the surface leading to more pinholes on the surface of Spiro-OMeTAD[20] and changing the perovskite film toward more n-doping and raising the surface potential.[21] Moreover, it could even pass through the perovskite layer and accumulate at the surface of the ETL, and higher Li-TFSi doping concentration could aggravate the hysteresis issue[22] and "burn-in" effect.[23] recently, some researchers indicated that Li^+ ions migration is also an essential factor affecting

the stability of PSCs at high temperatures.[24, 25] At present, the methods to eliminate the migration of Li^+ ions include adding MoS_2 with flower-like microstructures into spiro-OMeTAD acting as a powerful sorbent for Li+ ions;[26] doping reduced graphene oxide (rGO) to Spiro-OMeTAD to provide adsorption sites for Li^+ ions[27] and using a "cross-linkable" PCBM derivative to blocks this migration of Li+ ions.[23] However, there have been no reports of inhibition of ion mobility while passivating ETL.

Here we devise a strategy to passivate the defects at the interface between SnO_2 and perovskite while inhibiting Li^+ ions migration using the molecule 3,5-bis(fluorosulfonyl)benzoic acid (FBA). The carboxyl group in FBA acts as an effective multifunctional passivating agent at the interface between SnO_2 and perovskite due to filling oxygen vacancies and reducing the -OH group. Moreover, FBA optimizes the ETL's surface energy and flatness, leading to a larger perovskite grain size. Additionally, the FBA passivation layer modifies the work function of the SnO_2 with a favorable energy level difference between the perovskite and ETL, significantly improving the charge collection and transport properties in the device, resulting in a higher *V*oc and fill factor (FF). Finally, the fluorosulfonyl group can anchor Li^+ ions, thereby minimizing hysteresis and enhancing the device's stability.[28] Thanks to these favorable synergistic effects, the device based on FBA passivation achieved a high PCE of 24.26%. Moreover, the unencapsulated devices show better moisture-resistance stability and operation stability performance.

2. Result and discussion

2.1 FBA as SnO_2 passivation layer

The device with an ITO/SnO_2/$FAPbI_3$/Spiro-OMeTAD/MoO_3/Ag planar structure and the structure of 3,5-bis(fluorosulfonyl)benzoic acid is shown in **Figure 1a**. The detailed device performance is summarized in **Figure 1b** and **Table S1.** EQE spectra (**Figure S1**) show slight improvement, as seen in the short-circuit current density (J_{SC}). However, the open circuit voltage (V_{OC}) is significantly increased from 1.08V to 1.13V. As shown in the J–V curves (**Figure 1c**), the FBA passivation layer delivers higher performance, increasing the PCE from 22.28% to 24.26%. Additionally, the hysteresis issue is also inhibited but not eliminated. Moreover, the higher FF indicates better charge transport (higher shunt resistance) and efficient charge extraction through the contacts (lower series resistance).[29]

The first critical issue for the FBA to have these properties is to ensure the FBA molecule's orientation. Through first-principles density functional theory (DFT) calculations, the binding energy of perfect SnO_2 and FBA molecules in three different adsorption conditions, including an Sn-atom, hollow, or O-atom site **(Figure 1d** and **Figure S2a-b**), can be calculated as -0.39eV, -1.27eV and -3.21eV, respectively. However, in the actual situation, some traps mentioned above inevitably exist in the SnO_2 ETL layer. The binding energies of the FBA molecule and SnO_2 with -OH groups and O vacancy were calculated as -3.54 and -0.43 eV, shown in **Figure 1e** and **Figure S2c**. On the other hand, the binding energy of the FBA molecule and $FAPbI_3$ in different adsorption methods also can be achieved. (**Figure 1f** and **Figure S3a-c**). The maximum binding energy condition is FBA molecules with Pb atom, reaching -5.17 eV, as shown

previously,[30] indicating that the fluorosulfonyl group could coordinate with lead atoms to improve the stability of the devices. All the DFT results are shown in **Table S2**. On the other hand, through the sum-frequency generation spectroscopy (SFG) result in **Figure S4,** we observe that the peak of -OH groups found at 3200-3500 wavenumbers [31] decreases with the increasing immersion time of SnO_2 in FBA, proving that the carboxyl group bind to SnO_2. Therefore, these results demonstrate that the fundamental molecular orientation of FBA is that -OH is found to bind to tin oxide, while the sulfonic fluoride group is bound to the perovskite layer.

Secondly, X-ray photoelectron spectroscopy (XPS) is conducted to investigate how the electronic structure of SnO_2 changes with the addition of FBA. **Figure 2a** shows the whole spectra of SnO_2 and SnO_2-FBA. For the SnO_2-FBA spectra, some new peaks, including F 1*s* and S 2*p,* are detected. Moreover, in Sn 3*d* orbital (**Figure S5**), the peaks of FBA shift to the direction of higher binding energy with 0.2 eV (exceeds the instrument uncertainty), illustrating the presence of extra electrons around an Sn atom.[32] This evidence supports that the FBA molecules bind to the SnO_2 film surface. For the O 1*s* orbital, the binding energies at 530.2, 530.8, and 531.8 eV are attributed to Sn-O, surface-absorbed hydroxyl groups, and an O vacancy. O vacancy is the most typical charge state in SnO_2[33], and -OH groups could result in traps during the SnO_2 film-fabrication process, leading to lower device performance.[4] The defect percentage (calculated as $\frac{O_v+O_{-OH}}{O_{all}}$) shows a noticeable decrease from 58.4% to 41.4%, as measured in (**Figure 2b,c**), and shown in **Table S3**. The excellent passivation performance of FBA is due to carboxylic acid forming an ester bond with SnO_2 via the esterification

reaction[34] and react with both tin and oxygen dangling bonds on the SnO_2 surface, thereby passivating the surface with high coverage and reducing surface recombination.[8] Moreover, from the absorption spectra and transmission spectra data of each ETL, the effect of the FBA passivation layer on optical properties could be ignored **(Figure S6)**.

Lastly, inserting the FBA interfacial layer between ETL and the perovskite layer can improve the crystal quality and film coverage of perovskite film. The ETL must balance hydrophilicity and hydrophobicity to form a uniform film with a large grain size because the substrate is over-hydrophilic; although the film uniformity increases, the grain size tends to be smaller due to the high density of nuclei. On the other hand, the perovskite film could not completely cover the hydrophobic substrate, resulting in pinholes in the film.[36] As seen from the water contact angle in **Figure S7**, the water contact angle of SnO_2 is 5.4°. The water contact angle is also increased with the ascension of FBA precursor concentration. When the concentration of FBA precursor reaches 0.1mg/ml, the water contact angle is 16.4°. Moreover, from top-view scanning electron microscope (SEM) images in **Figure 2d-e**, the average grain size of the perovskite film based on SnO_2-FBA (2.13 μm) is much larger than that of the film on pristine SnO_2 (1.61 μm). **Figure 2f** demonstrates the statistical distribution of grain sizes of the perovskite film deposited on different ETL. These results confirm that suitable surface energy is achieved by introducing the FBA passivation layer. However, a higher concentration of FBA precursor (0.5 mg/ml) could cause grain boundary defects and pinholes in the perovskite film, as shown in **Figure S8**. Through the atomic

force microscopy (AFM) images of the FBA layer with different concentrations **(Figure S9)**, the agglomeration phenomenon can be observed when the FBA concentration is over 0.3mg/ml. It could be the reason for grain boundary defects and pinholes in the perovskite film. Moreover, the performance demonstrated in **Figure S10** and **Table S4** also proves that the moderate concentration of FBA (0.1 mg/ml) is beneficial for crystallization. Hence, from the SEM images, AFM results, and performance of the device, 0.1 mg/ml FBA concentration should be more appropriate. The cross-section SEM image (**Figure S11**) illustrates that the interface between SnO_2-FBA ETL and the perovskite layer is uniform and pinhole free. Additionally, from the atomic force microscopy (AFM) images (**Figure S12**), the surface roughness with the FBA passivation layer is significantly reduced, indicating the FBA could fill the nanopores on the surface of SnO_2, thus enhancing the flatness and mobility of SnO_2 ETL. Moreover, from the root means square (RMS) roughness of each perovskite film (**Figure S13**), the parameter barely changed, indicating that the morphology of perovskite film has not changed basically. The modified ETL's extraction properties are also improved as measured using photoluminescence (PL). From the PL curves shown in **Figure 2g**, the perovskite film on SnO_2-FBA shows the best PL quenching phenomenon thanks to better carrier extraction capacity. For the time-resolved photoluminescence (TRPL) of pure perovskite film (**Figure 2h**), two regimes can be distinguished: a carrier density-dependent lifetime at high TRPL signals (short delay times) and a constant lifetime at low TRPL signals (long delay times). However, it has been clearly shown by Kirchartz that we cannot use simple exponential lifetimes to

decouple the effects in the bulk and at the interface.[37] Instead, we employ the differential lifetime to distinguish these effects. The differential lifetime is defined as:

$$\tau_{PL} = (-\frac{1}{m}\frac{d\ln(\varphi_{PL})}{dt})^{-1}$$

where, $\varphi_{PL}(t)$ is the TRPL intensity at a given time after the pulse excitation, and the m is a factor related to the injection level. For high-level injection, m can be set to 2, and the perovskite layer can be assumed to be intrinsic or sufficiently low-doped.[37] **Figure S14** shows the TRPL intensity results, indicating increased interfacial electron transfer due to the presence of the FBA-modified ETL. Moreover, it is advantageous to plot the lifetime as a function of the quasi-Fermi level splitting $\Delta E_F = k_B T \ln(\Delta n^2 / {n_i}^2)$, where $k_B T$ is the thermal energy, Δn the excess carrier density, and n_i the intrinsic carrier density. Hence, carrier density is the most significant factor in analyzing recombination and extraction processes. We use the fact that the PL intensity scales with ΔE_F according to

$$\varphi_{PL} \propto \exp(\frac{\Delta E_F}{k_B T})$$

implying that ln (φ_{PL}) can be used as a relative measure of the quasi-Fermi level splitting shown in **Figure 2i**. Here, a density-dependent part can be contributed to direct radiative recombination, which could be illustrated as a second-order process that scales with $k_{rad}\Delta n^2$ (k_{rad} is the radiative recombination coefficient). The constant part is associated with the slower recombination via traps, which, according to Shockley Read Hall (SRH) statistics, resemble a pseudo-first-order process, and the plateau corresponds to an effective SRH lifetime in bulk.[38] On the other hand, for the samples with the ETL, the fast decay component represents the extraction of charge carriers at

the interface. At longer times, the decay is more rapid than for the perovskite-only film, indicating an additional recombination channel, which can be attributed to interfacial recombination.[39] In **Figure 2i**, The plateau of τ_{PL} In this case, the samples with ETL is given by a complex interplay of the bulk SRH lifetime and the surface recombination velocity S of electrons at the ETL. Hence, the surface recombination velocity S can be calculated using

$$\tau_{\mathrm{SRH,eff}} = (\frac{1}{\tau_{\mathrm{SRH,bulk}}} + \frac{S}{2d})^{-1}$$

where d is the thickness of the perovskite layer, which can be obtained from **Figure S11**, and the related results are shown in **Table S5**. Hence, the FBA passivation layer increases the surface recombination velocity, a measure of the electron extraction from the active layer to the electrode, from 35 to 409 cm/s, indicating that most carriers will be more easily extracted through the modified interface.

2.2 FBA anchored Li^+ ions

Another interesting phenomenon is that J–V hysteresis was modulated by the FBA-modified SnO_2 shown in **Figure 1c,** and the pre-voltage bias is introduced to investigate this phenomenon. **Figure 3a-b** delivers the J-V curve performance under different voltage bias conditions, including 1.5V forward and 1.5V reverse bias. **Table 1** shows the related parameters, and the hysteresis index (HI) can be calculated as the following equation:[40]

$$HI = (PCE_{Reverse} - PCE_{Forward})/PCE_{Reverse}$$

With a 1.5V forward pre-bias, the device in the first scan condition shows the best

performance after removing the bias. Moreover, with the increased number of scans, V_{OC} and FF decrease. On the other hand, with a 1.5V reverse pre-bias, the device performance is improved with the number of scans. **Figure 3c** demonstrates the device performance with FBA after different scan times. With the increased number of scans, the FF of the forward direction scan shows an upward trend, and the reverse direction scan is stable. However, with the increasing scan times, the device performance with ITO/SnO2/PVSK/Spiro/Ag structure is decreased. In terms of this issue, ion migration is usually considered the main reason for the hysteresis issue. Therefore, Time-of-Flight Secondary Ion Mass Spectrometry (ToF-SIMS) and XPS are used to detect the condition and concentration of each ion in the whole device. The SIMS results are shown in **Figure 3d**. As mentioned above, the change in Li^+ ion concentration is the most pronounced for the device with/without the FBA layer.

Additionally, the Li^+ ions accumulated in the interface and bulk of SnO_2 due to its high Li^+ affinity[41] and K^+ in the SnO_2 diffusion into the Spiro-OMeTAD layer provides intracellular ion equilibration.[42] For the original device, the concentration of Li^+ ions in the SnO_2 layer is unchanged concerning the device with 50 times forward and reverse scans. It is worth mentioning that a Li^+ ion peak at the interface between MoO_x and Spiro layer is also observed for the pristine device, which disappeared after 50 forward and reversed scans, indicating Li^+ ion migration under the applied test voltage. However, using SnO_2-FBA as the ETL, the concentration of Li^+ ions increase by approximately an order of magnitude after 50 times forward and reverse scans. Moreover, more Li^+ ions accumulated in the ETL and perovskite layer interface,

indicating that the FBA molecular layer can anchor the Li^+ ions.

Moreover, we also investigated the influence of FBA concentration. As shown in **Figure 3e**, 0.1mg/ml is enough to anchor the Li^+ ions. On the other hand, we also used a negative ion gun to investigate the FBA layer (**Figure S15**). From the ToF-SIMS results using a negative ion gun, S- and F- ions show a peak in the interface of SnO_2 and the perovskite layer. Moreover, by observing the characteristic elements of FBA, including SO^-, SO_2^-, and 34S at the interface between the SnO_2 and the perovskite layer, we show that FBA self-assembles on the SnO_2 surface. From these results, it can be concluded that for the device based on SnO_2 ETL, the Li^+ ions in the device could move back and forth across the whole device under different bias conditions, negatively influencing its performance. However, for the device with the FBA passivation layer, Li^+ ions are anchored by the SnO_2-FBA ETL, resulting in negligible hysteresis.

To further explore the FBA layer and its ability to anchor Li^+ ions, we fabricated two devices with Li-free HTL and Li-doped HTL. Then the electrodes, HTL, and perovskite layer are removed after 50 times forward and reverse scans. The XPS spectra of the residual SnO_2 ETL for each device is shown in **Figure 3f and 3g.** For the SnO_2-FBA film, an extra peak could be observed at 169.6 and 170.8 eV in the S 2*p* orbit, indicating the 2*p* 3/2 and 2*p* 1/2 characteristic peak of the $-C_6H_3-(SO_2F)_2$ group (S-F bonds).[43] However, the SnO_2-FBA layer from LiTFSI doped device (SnO_2-FBALi) film, due to Li+ ions in HTL immigration, the S 2*p* 3/2 characteristic peak moves to 168.5eV, corresponding to $-C_6H_3-(SO_2Li)_2$ formation.[44] Moreover, in Li 1*s* orbit and F 1*s* orbit (**Figure S16 and Figure 3h**), the peak at 55.7eV and 685eV could prove the

formation of LiF [45] due to the bond energy of S-F (284kJ/mol) being far less than C-F (485kJ/mol).[46] Moreover, as shown in Figure 3c, the SnO_2-FBALi layer is suitable for enhancing performance. The reason that SnO_2-FBALi ETL becomes better after Li^+ ions are anchored is analyzed from an energy band perspective. The work function and valence band can be obtained from the ultraviolet photoelectron spectroscopy (UPS) of the secondary electron cut-off and Fermi edge (**Figure 4a**). Inverse photoemission spectroscopy (IPES) is used to accurately estimate the electron affinity (EA) of perovskite and each ETL, shown in **Figure S17** and **Figure 4b**. From the IPES data, the EA of SnO_2, SnO_2-FBA, and SnO_2-FBALi are 3.63, 4.37, and 3.97eV, respectively. According to these results, the schematic description of the interface band bending of the ETLs and perovskite layer before and after contact are illustrated in **Figure 4a-c.** Because the EA of SnO_2 (3.67 eV) is lower than that of the perovskite layer (3.78 eV) before contact, the CB of SnO_2 bends upwards, and the CB of the perovskite layer bends down when brought into contact. Hence, since the energy level offset $\boldsymbol{\Delta E = E_{CB}^{FAPbI3} - E_{CB}^{SnO2}}$= -0.11 eV, the energy loss will cause lower V_{OC}. Furthermore, some electrons will be stuck at the interface leading to the possibility increased interfacial recombination. However, for the other two ETLs, the situation is the opposite. For the SnO_2-FBA ETL, the bending orientation is opposite compared to SnO_2 ETL, and ΔE increases to +0.59 eV. This mean that there will be a diffusion barrier for electrons at this interface. However, one thing to note is that pure SnO_2-FBA ETL is nonexistent in a real device, since Li^+ ions will always be present due to the spiro doping. When the Li^+ ions anchore to the FBA, the ΔE decreases from +0.59 to +0.19 eV, which would

lower the energy-loss for the electron transfer over this interface, thereby enhancing V_{OC} of the devices.

Therefore, the appearance shown in **Figure 3a-b** could also be explained that when the device is on the 1.5V forward pre-bias, Li^+ ions accumulate at the SnO_2 ETL layer, improving the built-in voltage. A lower built-in voltage means carriers are more difficult to extract since the electric field is lowered and possibly inverted.[51] On the other hand, a reverse pre-bias drives Li^+ ions away from the SnO_2 layer, and after removing the reverse pre-bias, the Li^+ ions will accumulate at the SnO_2 layer with more scans. Therefore, the performance of the devices is enhanced, and the hysteresis issues caused by Li^+ ions immigration is eliminated.

2.3 Performance of the PSCs with FBA passivation layer

2.3.1 Electric properties of the PSCs with FBA passivation layer

A series of electrical characterizations were performed to elucidate further the possible mechanism responsible for the enhancement of V_{OC} and FF. The capacitance-voltage (C–V) measurements were also taken to evaluate the built-in potentials (V_{bi}) of each device (**Figure 5a**). The V_{bi} is increased from 1.05 V to 1.08 V for the device with FBA passivated layer. A higher V_{bi} is favorable for extracting charge carriers from the device.[52] Another noticeable feature in the Mott-Schottky plots is C^{-2} of the FBA device is prominently higher than the control device, as would be expected when the FBA has anchored Li+-ions (chemical capacitance). Electrical impedance spectroscopy (EIS) also determined the charge transfer dynamics in PSCs (**Figure 5b**). The fitting

results in **Table S6** show that the device based on SnO_2-FBA ETL offers considerably higher charge recombination resistance values (R_{rec}) due to the reduced interfacial defect-assisted traps compared with the optimized device. The diode ideality factor is another good index to check the carrier recombination mechanism in the device. **Figure 5c** shows the plot of the V_{OC} versus the common logarithm of light intensity, and the light ideality factor (n) can be calculated as follow:

$$V_{oc} = \frac{nkT}{q}\ln(\frac{I_L}{I_0} + 1)$$ [53]

Hence, the light ideality factor of the device based on SnO_2 and SnO_2-FBA is 1.81 and 1.42, respectively, suggesting that defect-assisted charge recombination is significantly reduced in the FBA-based device.

2.3.2 Stability studies of the PSCs with FBA passivation layer

We also detected the stability of the devices based on SnO_2-FBA. **Figure 5d** and **Figure S18** show the operation stability of each type of device. Compared with the control devices, the devices with the FBA passivation layer offer better stability. After 1000 h continuous working hours, the PCE still could maintain over 80% of its initial performance when using FBA as a passivation layer, while the control devices dropped to 60% of their initial PCE. Moreover, we could also observe an apparent burn-in phenomenon for FF and PCE of control group devices. However, this issue is significantly inhibited for the passivated devices due to eliminated Li^+ ions migration, which is outside the scope of this paper and is discussed elsewhere.[23] Moreover, the air stability is also investigated and shown in **Figure 5e**. The unsealed FBA passivated

device showed a noticeable increase in stability and retained more than 80% of the initial PCE after 1000 h, while the control device rapidly dropped to ~50% of its initial value. To detect the fundamental reason for improving stability, XPS is used to inspect the state of the perovskite crystal. We also move the electrode and HTL of the aged device for each type of device and investigate the state of the perovskite layer. From the XPS spectrum of Pb 4*f* orbit (**Figure 5f**), the peak of Pb^0 in Pb 4*f* 5/2 and Pb 4*f* 7/2 orbit at approximately 141.5 and 136.5eV can be observed clearly for the control group device, illustrating that the chelation of -SO_2F indeed could make perovskite films stable and robust against moisture, light, and thermal stresses due to the undercoordinated Pb^{2+} or Pb clusters readily coordinates with S=O donating a pair of nonbonding electrons,[16] which consist with our DFT results. Finally, we also checked the stability of the devices under continuous scanning conditions (**Figure 5g**); the device with the FBA passivation layer shows excellent constant scanning stability compared with the control group device. Hence, it can be concluded that inhibiting ions migration is the main reason for eliminating hysteresis and improving continuous test stability. However, the decrease of defect density in the bulk and buried interface and the alignment of energy level are factors that cannot be ignored.[54]

3. Conclusion

In summary, we reported a hysteresis-free perovskite solar cell with a high PCE of 24.26% using a bridged molecule FBA. Firstly, we find that FBA passivates the trap

states on the SnO_2 film surface and achieves energy level matching, thereby enhancing the electron extraction as seen through an increased surface recombination velocity S. This leads to better FF and increases V_{bi}. Secondly, the FBA adjusting the surface energy of the ETL substrates is profitable for forming high-quality perovskite film with enlarged grain size and reducing the defect density of perovskite films. Finally, the sulfonic fluoride groups anchor Li^+ ions in the ETL, as demonstrated in the TOF-SIMS results and lower hysteresis phenomenon in the J-V curves. Meanwhile, the devices with FBA interfaces also exhibited improved moisture and operational stability. The PCE of the device remained over 80% of initial values under prolonged operation in humidity, with a minimized burn-in phenomenon. Li-TFSI is commonly used in high-performance n-i-p devices as an additive in the HTL. Hence, understanding the effect of the diffusion of Li^+ helps design and fabricate high-performance and hysteresis-free PSCs.

4. Experimental Section

Materials:

PbI_2, Formamidinium iodide (FAI), Lithium bis(trifluoromethanesulphony)imide (LiTFSI), Pyridine,4-(1,1-dimethylethyl)-(t-BP) and Spiro-OMeTAD were purchased from Xi'an Polymer Light Technology Corp`, dimethylformamide (DMF, purity>99%), dimethyl sulfoxide (DMSO, purity>99%), isopropanol (IPA, purity>99%)and chlorobenzene (CB, purity>99%) were purchased from J&K scientific. The SnO_2 colloid solution (tin (IV) oxide, 15 wt% in water) was purchased from Alfa Aesar, and

the 3,5-bis(fluorosulfonyl)benzoic acid (FBA) was purchased from Aladdin (99.9%).

Instruments and characterization

Solar cells' current density-voltage (J-V) characteristics were measured with a Keithley 2400 source meter in an N_2 glove box under a simulated sun AM 1.5 G (Newport VeraSol- 2 LED Class AAA Solar Simulator) using a mask with 0.0625cm^2. SEM images were gained by a field-emission scanning electron microscope (S-4800) under an accelerating voltage of 10 kV. The atomic force microscopy images of the films of SnO_2 were studied using a Veeco Dimension 3100 instrument at the ambient temperature in tapping mode. The X-ray and ultraviolet photoelectron spectroscopy (XPS and UPS) measurements were conducted at a PHI 5000 VersaprobeII system. The electrochemical impedance spectra were measured using an Autolab electrochemical workstation (Autolab PGSTAT 302N, Metrohm Autolab B.V.) The absorption curves of the sample were analyzed by UV–VIS spectrometer (Lambda 750, PerkinElmer). Photoluminescence (PL) and time-resolved photoluminescence (TRPL) of solar cells were tested by a home-built defects imaging system (LBIC). The time-of-flight secondary ion mass spectrometry (TOF-SIMS 5-100) was measured with the pulsed primary ions from a Cs+ (2 keV) liquid-metal ion gun for sputtering and a Bi+ pulsed primary ion beam for analysis (30 keV). Electrical impedance spectroscopy (EIS) and Mott-Schoktty (M-S) measurements were carried out on the electrochemical workstation (PGSTA302N). The EIS measure conditions were under dark and applied bias at open voltage. The frequency range is 0.1 Hz-10 MHz. The M-S plot

measurement conditions were determined to be a 10 kHz frequency. Operational stability of the cells was performed on a multi-channel solar cell performance decay testing system ((PVLT-G8001M, Suzhou D&R Instruments Co. Ltd.) inside an N_2-filled glove box (H_2O < 10 ppm, O_2< 10 ppm), and the cells were illuminated with a white LED light (D&R Light, L-W5300KA-150, Suzhou D&R Instruments Co. Ltd.) at a simulated one sun intensity (the initial short current equals to the JSC measured under standard condition). The cell's performance was measured by I-V sweeping from 1.2 V to -0.2 V, with a step of 0.02 V. The temperature was set at 25 ℃. The cells' current density-voltage (J-V) characteristics were measured periodically, and the maximum power output point (MPP) was calculated automatically. An external resistor that matches the MPP point ($R = I_{max}/V_{max}$) was then attached to the cells in between *J-V* sweepings according to the *J-V* sweeping results so that the recorded PCE decay curves directly reflect the performance decay of the cells under the simulated operational situation.

Preparation of the solution

The SnO_2 colloid solution (15 wt%) was diluted to the concentration of 3 wt% by deionized water. The FBA solution was prepared by dissolving 0.1mg FBA into 1ml IPA. The $FAPbI_3$ precursor solution was prepared as in our previous work.[55] The OAI solution was prepared by dissolving 5mg OAI into 1 ml IPA. The Spiro-OMeTAD solution was prepared by dissolving 72.3 mg Spiro-OMeTAD into 1 ml CB followed

by the addition of 17.5 μL Li-TFSI (520 mg/mL in acetonitrile) and 29 μL t-BP. Both OAI and Spiro-OMeTAD were stirred overnight at room temperature in the glove box.

Solar cell fabrication

ITO glass was cleaned by ultrasonic cleaning through detergent, DI water, acetone, and isopropanol for 30 min, respectively. Before use, the ITO substrate was cleaned with UV Ozone for 30 min. Then the substrate was spin-coated with a thin layer of SnO_2 nanoparticles from the SnO_2 colloid solution at 4000 rpm for 30 s with an accelerated speed of 2000 rpm. Then the substrate was annealed in ambient air at 150 ºC for 30 min.

For FBA passivation layer, the FBA solution was coated on SnO_2 layer with 5000rpm for 30s. Then the films were annealed at 90 °C for 10 min.

For $FAPbI_3$ active layer, the spin rate of this step is 5000 rpm for 30 s with an accelerated speed of 5000 rpm. During the end of 10-12s, 300 μL of CB was drop-coated to treat the perovskite films, and then the perovskite films were annealed at 150 °C for 15 min and 100°C for 15min. Then the film was washed with IPA by dropping several drops at 3000rpm and heated at 100°C for 1min.

After cooling to room temperature, the OAI solution was coated on perovskite films at 5000rpm for the 30s with an accelerated speed of 5000 rpm. Then the Spiro-OMeTAD solution was coated at 3000 rpm for 30 s with an accelerated rate of 3000 rpm.

Finally, 8 nm thick MoO_3 and 80 nm thick Ag were deposited on the Spiro-OMeTAD film by thermal evaporation with the rate of 0.3 Å/s and 2 Å/s.

DFT calculations

All calculations were carried out using the projector augmented wave method in the density functional theory framework (DFT) framework, as implemented in the Vienna ab-initio Simulation Package (VASP). The generalized gradient approximation (GGA) and Perdew–Burke–Ernzerhof (PBE) exchange functional was used. The plane-wave energy cut-off was set to 500 eV, and the Monkhorst–Pack method was employed for the Brillouin zone sampling. The convergence criteria of energy and force calculations were set to 10−5 eV/atom and 0.01 eV/Å, respectively. To explore the interactions between the organic molecule and SnO_2 or $FAPbI_3$ surfaces, including SnO_2 (110) or $FAPbI_3$ (001), the binding energies of the organic molecule on the SnO_2 or $FAPbI_3$ surfaces were calculated. The SnO_2 surface model was built by the 2×2 supercell of SnO_2 (110), and the $FAPbI_3$ surface model was built by the 2×2 supercell of FAPbI3 (001). A vacuum region of 15 Å is applied to avoid interactions between the neighboring configurations. DFT-D2 method accounted for the vdW interactions between the organic molecule and metal surface[56]. Here, the binding energies (Eb) were calculated by the energy difference of the system after and before binding[57]: Ea=E(molecule-slab)–E(molecule)-E(slab), where (molecule-slab), E(molecule) and E(slab) represent the DFT energies of the molecule adsorbed surface, the energy of an isolated molecule, and the energy of the clean SnO_2 or $FAPbI_3$ surface, respectively.

Acknowledgments

This research was funded in part by the Natural Science Foundation of the Jiangsu Higher Education Institutions of China Program (19KJB510059), Natural Science Foundation of Jiangsu Province of China (BK20180242), Jiangsu Science and Technology Program(BE2022023), the Suzhou Science and Technology Development Planning Project: Key Industrial Technology Innovation (SYG201924), Ministry of Science and Technology Project (G2021014029L), University Research Development Fund (RDF-17-01-13), and the Key Program Special Fund in XJTLU (KSF-P-02, KSF-T-03, KSF-A-04, KSF-A-05, KSF-A-07, KSF-A-18). This work was partially supported by the XJTLU AI University Research Centre and Jiangsu (Provincial) Data Science and Cognitive Computational Engineering Research Centre at XJTLU, and Jiangsu Key Laboratory for Carbon-based Functional Materials & Devices, Soochow University. The author Ivona Z. Mitrovic acknowledges the British Council UKIERI project no. IND/CONT/G/17-18/18.) The authors would like to acknowledge the Vacuum Interconnected Nanotech Workstation (Nano-X) of SINANO, CAS, for the online XPS/UPS characterization on the samples (Project No. A2107).

Author Contributions

L. Yin designed the experiment, fabricated the perovskite solar cells, analyzed the data, and wrote the original draft. C.Z Ding and H.B. Wang helped to analyze the energy level alignment. C.G. Liu helped to design the experiment. L.P. Zhang contributed to SEM images. W Zha helped to analyze the DFT data. Y.X Li contributed to PL data fitting. C.Z Ding and Y.F. Han contributed to EIS data

analysis. H.Z. Lin contributes to the SFG analysis. I.Z. Mitrovic, E.G. Lim, L. Yang, R. Österbacka, S.Wilken and C.Z. Zhao contribute to the revision of the original manuscript. L. Yin, with the help of C. Zhao, E.G. Lim and C.Q. Ma, designed the experiment and wrote the manuscript. All authors contributed to the interpretation and discussion of the results.

References

[1] Q. Jiang, Y. Zhao, X. Zhang, X. Yang, Y. Chen, Z. Chu, Q. Ye, X. Li, Z. Yin, J. You, *Nat. Photonics*, **2019**, 13, 460-466.

[2] D. Shi, V. Adinolfi, R. Comin, M. Yuan, E. Alarousu, A. Buin, Y. Chen, S. Hoogland, A. Rothenberger, K. Katsiev, Y. Losovyj, X. Zhang, P.A. Dowben, O.F. Mohammed, E.H. Sargent, O.M. Bakr, *Science*, **2015**, 347, 519.

[3] Y. Rong, Y. Hu, A. Mei, H. Tan, M.I. Saidaminov, S.I. Seok, M.D. McGehee, E.H. Sargent, H. Han, *Science*, **2018**, 361.

[4] Z. Dai, S.K. Yadavalli, M. Chen, A. Abbaspourtamijani, Y. Qi, N.P. Padture, *Science*, **2021**, 372, 618.

[5] L. Zhang, X. Pan, L. Liu, L. Ding, *J. Semicond.*, **2022**, 43, 030203.

[6] Available from: https://www.nrel.gov/pv/assets/pdfs/bestresearch-cell-efficiencies.20210401.pdf.

[7] K. Yoshikawa, H. Kawasaki, W. Yoshida, T. Irie, K. Konishi, K. Nakano, T. Uto, D. Adachi, M. Kanematsu, H. Uzu, K. Yamamoto, *Nat. Energy*, **2017**, 2, 17032.

[8] C. Altinkaya, E. Aydin, E. Ugur, F.H. Isikgor, A.S. Subbiah, M. De Bastiani, J.

Liu, A. Babayigit, T.G. Allen, F. Laquai, A. Yildiz, S. De Wolf, *Adv. Mater.*, **2021**, 33, 2005504.

[9] P. Zhu, S. Gu, X. Luo, Y. Gao, S. Li, J. Zhu, H. Tan, *Adv. Energy Mater.*, **2019**, 10, 1903083.

[10] X. Shi, R. Chen, T. Jiang, S. Ma, X. Liu, Y. Ding, M. Cai, J. Wu, S. Dai, *Sol. RRL*, **2020**, 4, 1900198.

[11] P. Wang, R. Li, B. Chen, F. Hou, J. Zhang, Y. Zhao, X. Zhang, *Adv. Mater.*, **2020**, 32, 1905766.

[12] H. Dong, J. Wang, X. Li, W. Liu, T. Xia, D. Yao, L. Zhang, C. Zuo, L. Ding, F. Long, *ACS Appl. Mater. Interfaces*, **2022**, 14, 34143-34150.

[13] H. Zhou, Q. Chen, G. Li, S. Luo, T.B. Song, H.S. Duan, Z. Hong, J. You, Y. Liu, Y. Yang, *Science*, **2014**, 345, 542-6.

[14] G. Yang, C. Wang, H. Lei, X. Zheng, P. Qin, L. Xiong, X. Zhao, Y. Yan, G. Fang, *J. Mater. Chem. A*, **2017**, 5, 1658-1666.

[15] C. Wang, C. Xiao, Y. Yu, D. Zhao, R.A. Awni, C.R. Grice, K. Ghimire, I. Constantinou, W. Liao, A.J. Cimaroli, P. Liu, J. Chen, N.J. Podraza, C.-S. Jiang, M.M. Al-Jassim, X. Zhao, Y. Yan, *Adv. Energy Mater.*, **2017**, 7, 1700414.

[16] Y. Dong, W. Shen, W. Dong, C. Bai, J. Zhao, Y. Zhou, F. Huang, Y.-B. Cheng, J. Zhong, *Adv. Energy Mater.*, **2022**, 12, 2200417.

[17] J.H. Noh, N.J. Jeon, Y.C. Choi, M.K. Nazeeruddin, M. Grätzel, S.I. Seok, *J. Mater. Chem. A*, **2013**, 1, 11842-11847.

[18] J. Luo, J. Zhu, F. Lin, J. Xia, H. Yang, JinyuYang, R. Wang, J. Yuan, Z. Wan, N.

Li, C.J. Brabec, C. Jia, *Chem. Mater.*, **2022**, 34, 1499-1508.

[19] X. Ren, L. Zhang, Y. Yuan, L. Ding, *J. Semicond.*, **2021**, 42, 010201.

[20] Z. Hawash, L.K. Ono, S.R. Raga, M.V. Lee, Y. Qi, *Chem. Mater.*, **2015**, 27, 562-569.

[21] C. Xiao, F. Zhang, Z. Li, S.P. Harvey, X. Chen, K. Wang, C.-S. Jiang, K. Zhu, M. Al-Jassim, *Matter*, **2020**, 2, 261-272.

[22] Z. Li, C. Xiao, Y. Yang, S.P. Harvey, D.H. Kim, J.A. Christians, M. Yang, P. Schulz, S.U. Nanayakkara, C.-S. Jiang, J.M. Luther, J.J. Berry, M.C. Beard, M.M. Al-Jassim, K. Zhu, *Energy Environ. Sci*, **2017**, 10, 1234-1242.

[23] C. Ding, L. Yin, J. Wang, V. Larini, L. Zhang, R. Huang, M. Nyman, L. Zhao, C. Zhao, W. Li, Q. Luo, Y. Shen, R. Österbacka, G. Grancini, C.-Q. Ma, *Adv. Mater.*, **2023**, 35, 2207656.

[24] T. Wang, Y. Zhang, W. Kong, L. Qiao, B. Peng, Z. Shen, Q. Han, H. Chen, Z. Yuan, R. Zheng, X. Yang, *Science*, **2022**, 377, 1227-1232.

[25] S. You, H. Zeng, Y. Liu, B. Han, M. Li, L. Li, X. Zheng, R. Guo, L. Luo, Z. Li, C. Zhang, R. Liu, Y. Zhao, S. Zhang, Q. Peng, T. Wang, Q. Chen, F.T. Eickemeyer, B. Carlsen, S.M. Zakeeruddin, L. Mai, Y. Rong, M. Grätzel, X. Li, *Science*, **2023**, 379, 288-294.

[26] L.-L. Jiang, Z.-K. Wang, M. Li, C.-H. Li, P.-F. Fang, L.-S. Liao, *J. Mater. Chem. A*, **2019**, 7, 3655-3663.

[27] X. Guo, J. Li, B. Wang, P. Zeng, F. Li, Q. Yang, Y. Chen, M. Liu, *ACS Appl. Energy Mater.*, **2020**, 3, 970-976.

[28] N.-G. Park, M. Grätzel, T. Miyasaka, K. Zhu, K. Emery, *Nat. Energy*, **2016**, 1, 16152.

[29] J. Peng, D. Walter, Y. Ren, M. Tebyetekerwa, Y. Wu, T. Duong, Q. Lin, J. Li, T. Lu, A. Mahmud Md, C. Lem Olivier Lee, S. Zhao, W. Liu, Y. Liu, H. Shen, L. Li, F. Kremer, T. Nguyen Hieu, D.-Y. Choi, J. Weber Klaus, R. Catchpole Kylie, P. White Thomas, *Science*, **2021**, 371, 390-395.

[30] S. Chen, Y. Deng, X. Xiao, S. Xu, P.N. Rudd, J. Huang, *Nat. Sustain.*, **2021**, 4, 636-643.

[31] R. Yi, Y. Mao, Y. Shen, L. Chen, *J. Am. Chem. Soc*, **2021**, 143, 12897-12912.

[32] J. Yan, Z. Lin, Q. Cai, X. Wen, C. Mu, *ACS Appl. Energy Mater.*, **2020**, 3, 3504-3511.

[33] Ç. Kılıç and A. Zunger, *Phys. Rev. Lett*, **2002**, 88, 095501.

[34] J. Chen, X. Zhao, S.G. Kim, N.G. Park, *Adv Mater*, **2019**, 31, e1902902.

[35] J.-L. Bredas, *Mater. Horiz.*, **2014**, 1, 17-19.

[36] J. Chung, S.S. Shin, K. Hwang, G. Kim, K.W. Kim, D.S. Lee, W. Kim, B.S. Ma, Y.-K. Kim, T.-S. Kim, J. Seo, *Energy Environ. Sci*, **2020**, 13, 4854-4861.

[37] L. Krückemeier, B. Krogmeier, Z. Liu, U. Rau, T. Kirchartz, *Adv. Energy Mater.*, **2021**, 11, 2003489.

[38] M. Liu, S. Dahlström, C. Ahläng, S. Wilken, A. Degterev, A. Matuhina, M. Hadadian, M. Markkanen, K. Aitola, A. Kamppinen, J. Deska, O. Mangs, M. Nyman, P. Lund, J.-H. Smått, R. Österbacka, P. Vivo, *J. Mater. Chem. A*, **2022**.

[39] M. Stolterfoht, C.M. Wolff, J.A. Márquez, S. Zhang, C.J. Hages, D. Rothhardt,

S. Albrecht, P.L. Burn, P. Meredith, T. Unold, *Nat. Energy*, **2018**, 3, 847-854.

[40] D.H. Kang and N.G. Park, *Adv. Mater.*, **2019**, 31, 1805214.

[41] Z. Su, Y. He, S. Liu, J. Li, X. Xiao, J. Nan, X. Zuo, *ACS Appl. Energy Mater.*, **2022**, 5, 10264-10275.

[42] C. Ding, R. Huang, C. Ahläng, J. Lin, L. Zhang, D. Zhang, Q. Luo, F. Li, R. Österbacka, C.-Q. Ma, *J. Mater. Chem. A*, **2021**, 9, 7575-7585.

[43] B.J. Lindberg, K. Hamrin, G. Johansson, U. Gelius, A. Fahlman, C. Nordling, K. Siegbahn, *Phys Scr*, **1970**, 1, 286-298.

[44] Y. Gao, T. Rojas, K. Wang, S. Liu, D. Wang, T. Chen, H. Wang, A.T. Ngo, D. Wang, *Nat. Energy*, **2020**, 5, 534-542.

[45] W.E. Morgan, J.R. Van Wazer, W.J. Stec, *J. Am. Chem. Soc*, **1973**, 95, 751-755.

[46] T.L. Cottrell, *The strengths of chemical bonds*. 1958: Butterworths Scientific Publications.

[47] M. Park, J.-Y. Kim, H.J. Son, C.-H. Lee, S.S. Jang, M.J. Ko, *Nano Energy*, **2016**, 26, 208-215.

[48] M. Kim, I.-w. Choi, S.J. Choi, J.W. Song, S.-I. Mo, J.-H. An, Y. Jo, S. Ahn, S.K. Ahn, G.-H. Kim, D.S. Kim, *Joule*, **2021**, 5, 659-672.

[49] Z. Xu, N. Li, X. Niu, H. Liu, G. Liu, Q. Chen, H. Zhou, *Energy Material Advances*, **2022**, 2022, 9781073.

[50] P. Guo, H. Zhu, W. Zhao, C. Liu, L. Zhu, Q. Ye, N. Jia, H. Wang, X. Zhang, W. Huang, V.A. Vinokurov, E. Ivanov, D. Shchukin, D. Harvey, J.M. Ulloa, A. Hierro, H. Wang, *Adv. Mater.*, **2021**, 33, 2101590.

[51] V.M. Le Corre, M. Stolterfoht, L. Perdigón Toro, M. Feuerstein, C. Wolff, L. Gil-Escrig, H.J. Bolink, D. Neher, L.J.A. Koster, *ACS Appl. Energy Mater.*, **2019**, 2, 6280-6287.

[52] L. Zhu, J. Shi, S. Lv, Y. Yang, X. Xu, Y. Xu, J. Xiao, H. Wu, Y. Luo, D. Li, Q. Meng, *Nano Energy*, **2015**, 15, 540-548.

[53] Q. Lou, Y. Han, C. Liu, K. Zheng, J. Zhang, X. Chen, Q. Du, C. Chen, Z. Ge, *Adv. Energy Mater.*, **2021**.

[54] D. Yang, R. Yang, K. Wang, C. Wu, X. Zhu, J. Feng, X. Ren, G. Fang, S. Priya, S. Liu, *Nat. Commun.*, **2018**, 9, 3239.

[55] L. Yin, C. Liu, C. Ding, C. Zhao, I.Z. Mitrovic, E.G. Lim, H. Wang, Y. Sun, Y. Han, Z. Li, L. Yang, C.-Q. Ma, C. Zhao, *Cell Reports Physical Science*, **2022**, 3.

[56] S.A. Grimme, J.; Ehrlich, S.; Krieg, H. A, *J. Chem. Phys*, **2010**, 132, 154104.

[57] X. Lv, Z. Xu, J. Li, J. Chen, Q. Liu, *Appl. Surf. Sci.*, **2016**, 376, 97-104.

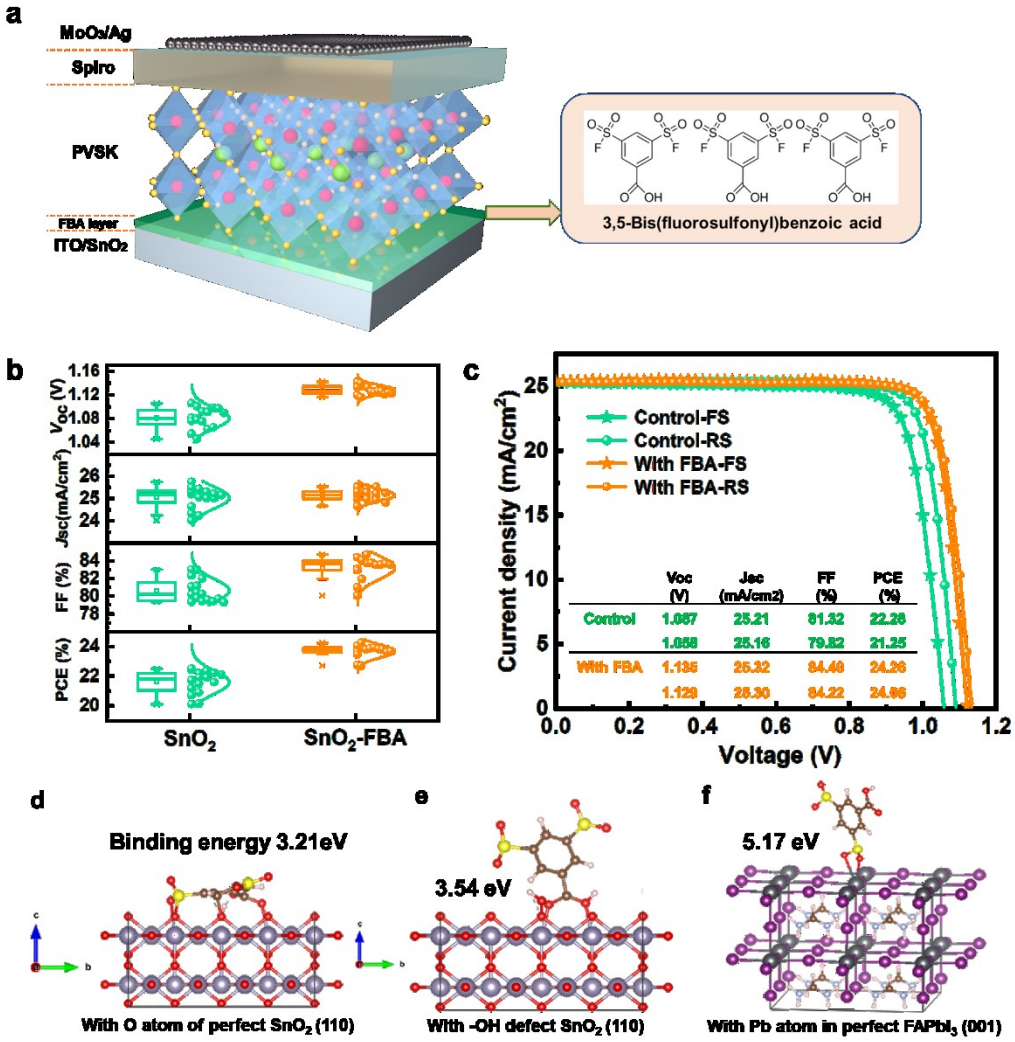

Figure 1. a) Schematic diagram of the passivation layer formed between the SnO_2 ETL and perovskite layer. b) Statistical distribution diagram of the performance of the control group and devices with the FBA passivation layer. c) J–V curves of devices based on SnO_2 and SnO_2-FBA ETL. Theoretical models of FBA molecular with different SnO_2 structures d) perfect structure e) with OH group traps. f) Theoretical models of FBA molecular with perovskite.

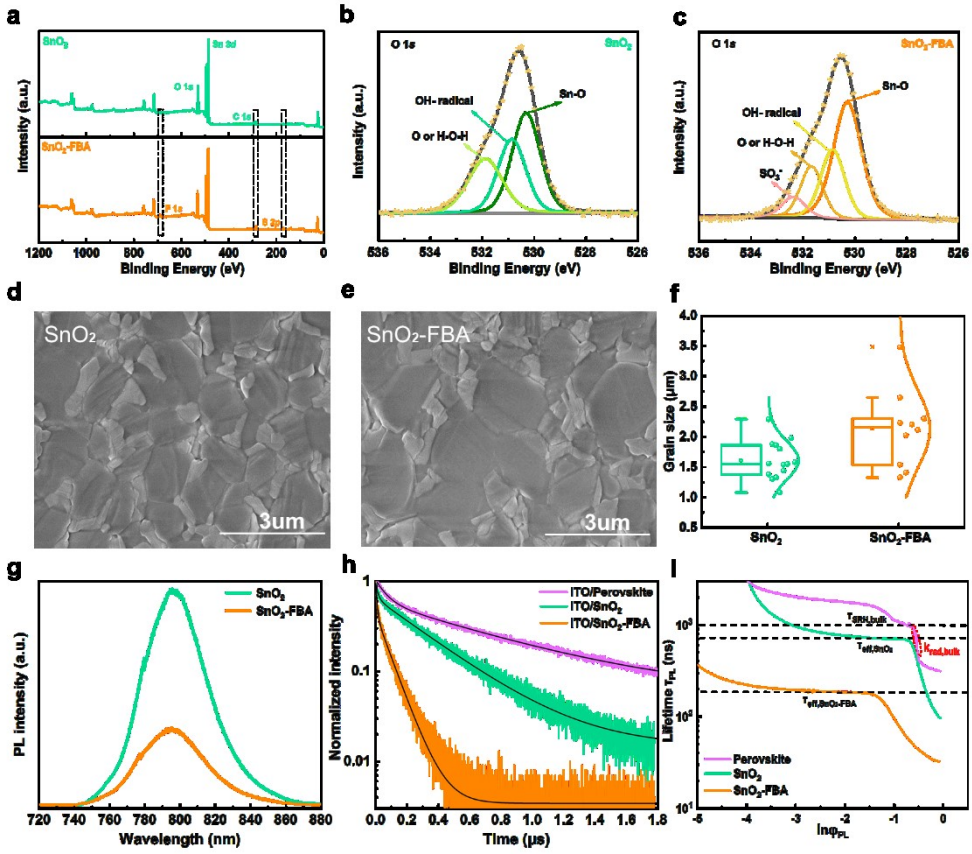

Figure 2. a) XPS full spectra of SnO_2 and SnO_2-FBA. b-c) XPS high-resolution spectra of SnO_2 and SnO_2-FBA in O 1*s* orbit. SEM images and box chart of grain size of perovskite films deposited on SnO_2 and SnO_2-FBA ETLs. d) SnO_2; e) SnO_2-FBA; f) box chart. g) PL and h) TRPL spectra of perovskite films deposited on SnO_2 and SnO_2-FBA ETLs. i) Differential lifetime as a function of the logarithm of the TRPL intensity

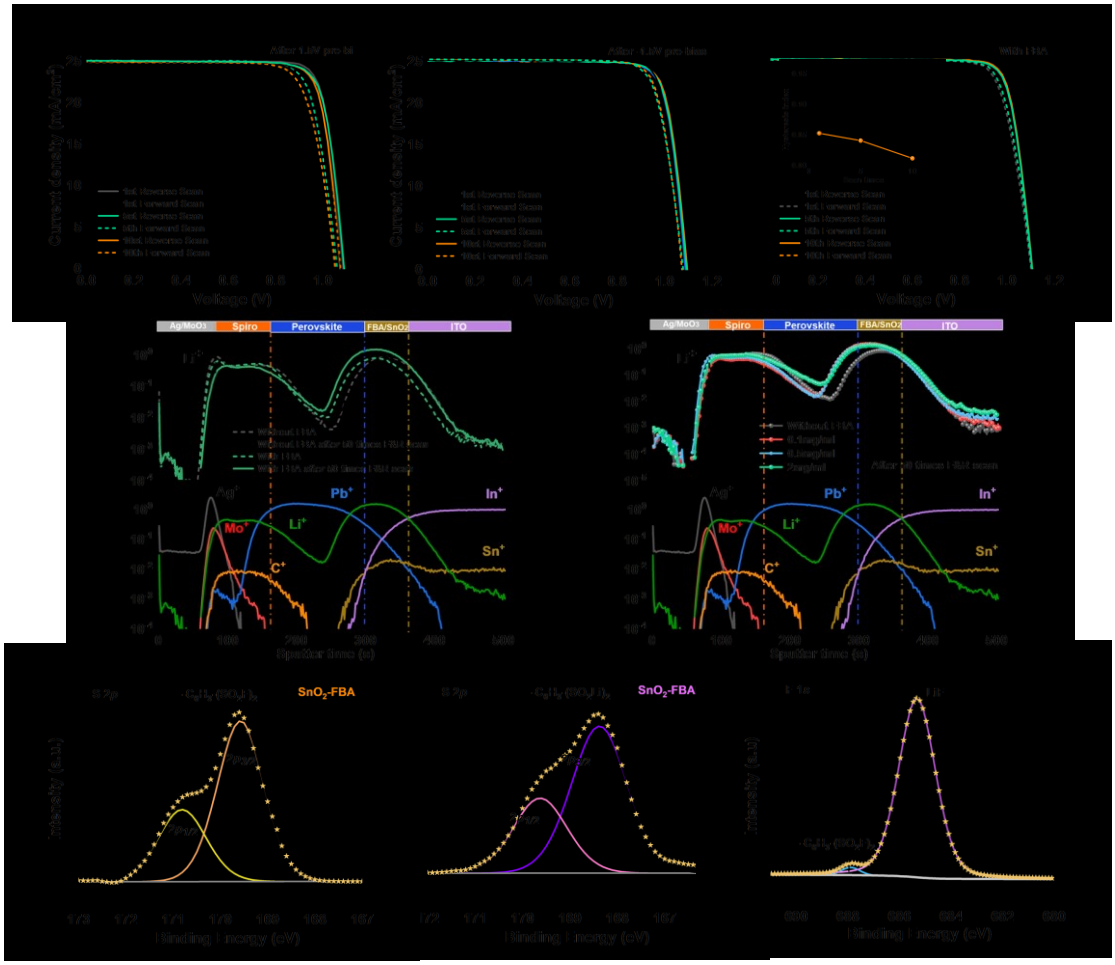

Figure 3. Reverse (solid) and forward (dash) *J–V* curves of control group device after pre-bias poling, 1st, 5th, and 10th scans. a) 1.5V pre-bias b) -1.5V pre-bias. c) Reverse (solid) and forward (dash) *J–V* curves for the device with FBA passivation layer with 1st, 5th, and 10th scans. d) ToF-SIMS data of devices deposited on SnO_2 and SnO_2-FBA ETLs; e) ToF-SIMS data of devices deposited on SnO_2-FBA ETL with different FBA concentrations. XPS high-resolution spectra of f) SnO_2-FBA and g) SnO_2-FBALi. h) High-resolution XPS spectra of F 1*s* orbit for SnO_2-FBALi ETL.

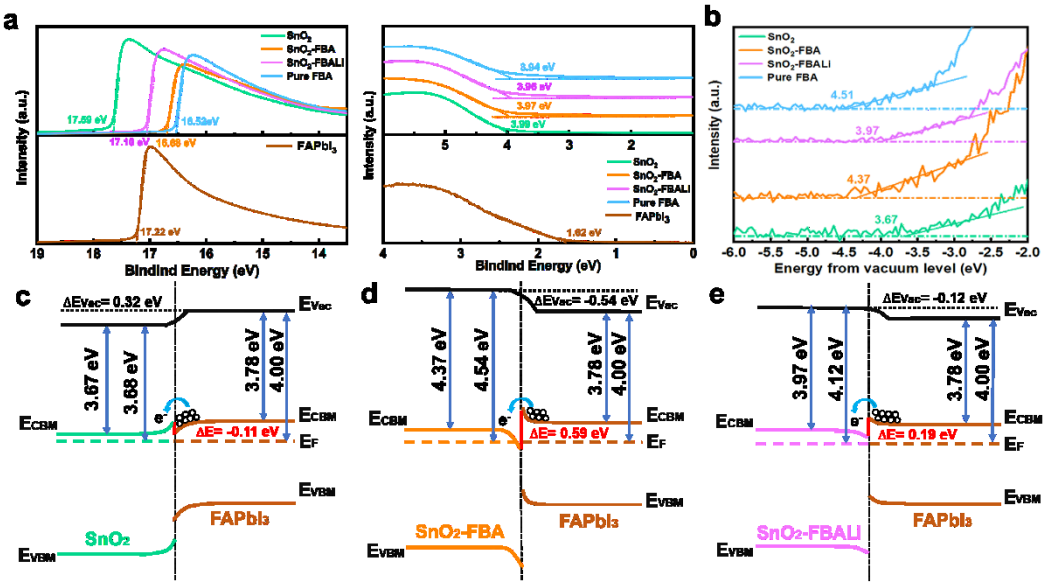

Figure 4. a) UPS spectra of secondary electron cut-off and valence bands of different ETL and perovskite layer. b) IPES spectra of SnO_2, SnO_2-FBA and SnO_2-FBALi. The schematic description of the interface band bending of c) SnO_2/$FAPbI_3$; d) SnO_2-FBA/$FAPbI_3$; and e) SnO_2-FBALi/$FAPbI_3$ before and after contact. The shift of vacuum energy level ($\Delta E_{Vac} = E_{Vac}^{FAPbI3} - E_{Vac}^{SnO2}$) and the energy difference between the CB of SnO_2 and $FAPbI_3$ ($\Delta E = E_{CB}^{FAPbI3} - E_{CB}^{SnO2}$) are shown in these figures directly.

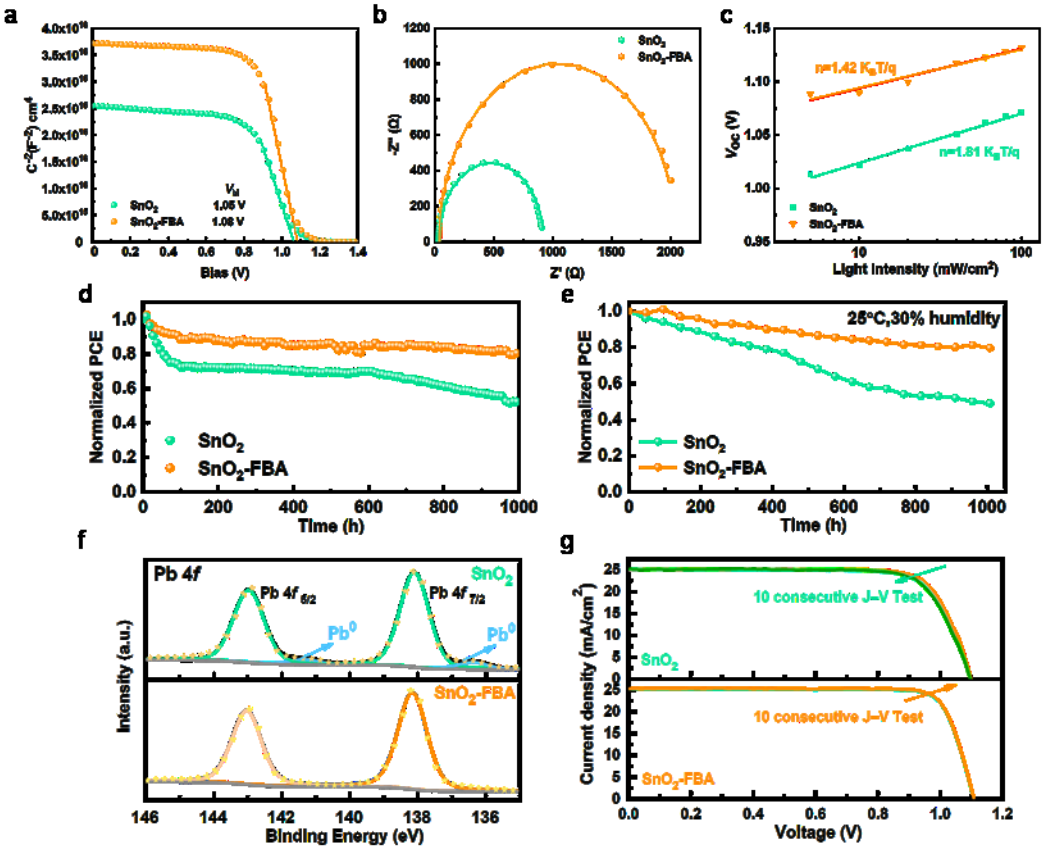

Figure 5. a) Mott–Schottky analysis at 1000 Hz, b) Electrical impedance spectroscopy (EIS) of PSCs, c) *V*oc versus light intensity, and Normalized averaged PCE of the corresponding devices in d) continuous operation condition; e) 25° C, 30% humidity. f) XPS high-resolution spectra of perovskite layer after 1000h operation test for corresponding devices. g) Continuous scanning stability of the device based on SnO_2 and SnO_2-FBA.

Table 1. Photovoltaic parameters of PSCs based on SnO_2 under voltage bias and PSCs based on SnO_2-FBA measured in both forward and reverse scan directions under AM 1.5 G illumination (100 mW cm^{-2}).

Test Condition	Times	Scan direction	V_{oc} (V)	J_{SC} (mA/cm^2)	FF (%)	PCE (%)	HI
1.5V bias	1st	Forward	1.118	25.04	79.68	22.30	0.059
		Reverse	1.127	25.10	83.85	23.72	
	5th	Forward	1.104	25.06	76.73	21.23	0.086
		Reverse	1.129	25.12	81.94	23.24	
	10th	Forward	1.095	24.96	73.23	20.01	0.109
		Reverse	1.117	25.03	80.32	22.46	
-1.5V bias	1st	Forward	1.115	25.09	74.78	20.92	0.112
		Reverse	1.122	25.22	83.23	23.55	
	5th	Forward	1.119	25.08	77.48	21.74	0.082
		Reverse	1.135	25.20	82.78	23.67	
	10th	Forward	1.114	25.16	79.22	22.20	0.063
		Reverse	1.137	25.23	82.63	23.70	
With FBA	1st	Forward	1.102	25.20	80.14	22.28	0.053
		Reverse	1.109	25.33	83.76	23.53	
	5th	Forward	1.103	25.21	81.05	22.53	0.041
		Reverse	1.107	25.30	83.92	23.50	
	10th	Forward	1.106	25.20	83.51	23.28	0.012
		Reverse	1.110	25.28	84.03	23.57	